International Journal of Solids and Structures 49 (2012) 1786–1801

Contents lists available at SciVerse ScienceDirect

International Journal of Solids and Structures

journal homepage: www.elsevier.com/locate/ijsolstr

A new type of stone dome based on Abeille's bond

M. Brocato [a,b,*], L. Mondardini [a]

[a] University Paris-Est, Laboratoire GSA – Géométrie Structure Architecture (Ecole nationale supérieure d'architecture Paris-Malaquais), 14 rue Bonaparte 75006 Paris, France
[b] University Paris-Est, Laboratoire Navier, 6 et 8 Av. Blaise Pascal 77455 Champs-sur-Marne, France

ARTICLE INFO

Article history:
Received 11 July 2011
Received in revised form 7 March 2012
Available online 6 April 2012

Keywords:
Stereotomy
Stone
Vault
Optimization
Parametrization

ABSTRACT

We deal with a new kind of stone spherical vaults, bonded adapting Joseph Abeille's 1699 patent for flat vaults. After the presentation of a parametric design procedure, we put forward a numerical model and propose a method to seek the optimal parameters. We conclude giving tools to process the information and produce fabrication outputs.

Most of the issues related to the stereotomy of the quoted system are solved; the automatic design of such vaults is made accessible starting from the choice of a topology and a few geometric parameters. A finite element model of the structure is put forward, sufficiently rich to nourish with numerical results the seek of optimality. A graphic representation of such results is proposed to characterize synthetically each structure's performances and compare tentatives to select the optimum.

Examples are given of optimal choices of the design parameters.

1. Introduction

In 1699 a bond for the construction of flat vaults was invented by Joseph Abeille (Gallon, 1735); an improved variant was proposed later by Sébastien Truchet. Both were presented and studied by Frézier (1737 reprint in 1980). These findings answered to the search for a stony building system that, made of shorter elements than the span, could cover a space with a flat ceiling. The thrust of any kind of standard vault, if flat, clearly blocked whatever straightforward applications of known stereotomic systems. Hence the importance, at their times, of Abeille's and Truchet's proposals.

The geometry of Abeille's flat vault is based on a square tiling obtained through translation and rotation of a single ashlar type, a polyhedron having two orthogonal cross sections (both vertical and passing through the centroid) in the shape of isosceles trapezia with the longer bases at opposite sides (see Fig. 1). Contrary to what happens in other stereotomic systems, this structure is conceived as the assembly of identical stone pieces leaving an inherent decorative pattern on the underside.

Truchet developed his design as an improvement of Abeille's, with interlocking shapes that leave no void on either surface of the vault and have ruled contact surfaces between stones.

Probably inspired by the proposals of timber frames that appeared previously in Villard De Honnecourt, Leonardo da Vinci, and Sebastiano Serlio, and in the contemporary work of John Wallis (these timber frames are called Serlio's floors in Emy (1837) and Yeomans (1997)), the flat vaults are structures that partake of the nature of nexorades (or reciprocal frames Baverel (2000), Baverel et al. (2000), Baverel and Nooshin (2007)) and of traditional vaults.

In fact, as already noticed by Frézier (1737 reprint in 1980), each ashlar, like a wooden beam in a Serlio's floor, supports two neighboring ashlars and is supported by two others. The support is not simple though as it happens for wooden timbers, because the inclination of the joints induces a side thrust. Thus, these vaults can discharge loads in compression as usually, but, thanks to the particular interweaving of stones—mimicking that of timbers in Serlio's, a bending resistance larger than standard can be obtained for unit thrust. As a consequence, a sufficient strength of the construction to withstand its self weight and the usual vertical loads was expected, together with an enhancement of the vault's intrados appearance.

The static performance of the system has recently been observed in experiments (Fleury, 2009).

If Abeille's and derived bonds were used to build only a few flat vaults in XVIII and XIX century's Spain (Rabasa-Dìaz, 1998; Nichilo, 2003; Uva, 2003), these systems have lately received a renewed attention for the design of curved surfaces (Etlin et al., 2008; Fallacara, 2006, 2009; Sakarovitch, 2006). Interesting geometric and structural issues emerge then from the need of adapting the bond on the surface. A routine to define the shape and arrangement of stones given the morphology of the vault has been proposed by the authors of this paper (Brocato and Mondardini, 2010, 2011), some unpublished variants are presented here. In addition, this paper focuses on the idea that a structural optimum can be sought

* Corresponding author at: University Paris-Est, Laboratoire GSA – Géométrie Structure Architecture (Ecole nationale supérieure d'architecture Paris-Malaquais), 14 rue Bonaparte 75006 Paris, France. Tel.: +33 (0) 155045654.

E-mail addresses: maurizio.brocato@paris-malaquais.archi.fr (M. Brocato), mondardini.lucia@gmail.com (L. Mondardini).

0020-7683/$ - see front matter © 2012 Elsevier Ltd. All rights reserved.
http://dx.doi.org/10.1016/j.ijsolstr.2012.03.036

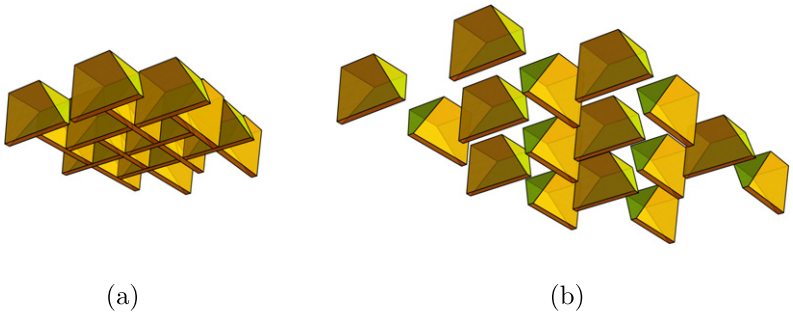

Fig. 1. Perspective views of a portion of an Abeille's flat vault: (a) mounted, (b) exploded. This vault is characterized by a smooth extrados and a carved intrados, nevertheless the bond is stable also if mounted upside-down.

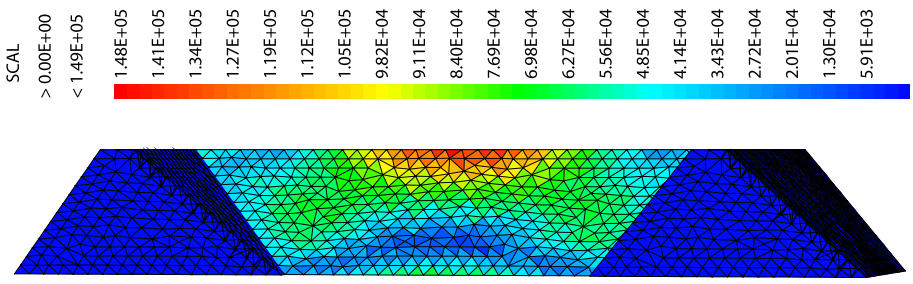

Fig. 2. Von Mises stresses [Pa] in the vertical cross section of a typical Abeille's flat vault ashlar resting on ideal smooth contacts on two fixed similar stones and bearing a vertical load of 50 kN equally distributed on top of it. The discharge arch and the tensile zone below are clearly observable; the highest stresses appear next to the upper surface, where the local effect of the applied load and the arch's thrust cumulate.

changing the parameters of the bonding and presents a method to derive it.

In a curved Abeille's bonding two features can be expected to merge: the catenary effect inherent with vaulted forms and the stacking timber effect proper to nexorades. Hence the guess that an optimum exists between a system where the former character dominates over the latter one and a system where the opposite condition takes place. Nexorades can in fact be seen as structures statically antithetical to arches, that can be named 'levery' as based on the principle of the lever instead than that of the inverted chain (Brocato, 2011).

Notice that Abeille's flat vault stability relies on thrust as it happens in standard vaulted systems, but—contrary to what occurs in these systems—here each stone withstand loads as a compressed deep beam. The inclination of the stone's faces makes in fact contact forces act out of the plane of the vault, with a resultant orthogonal to that plane larger, per unit of thrust, than standard. Actions in the stone are those typical of bending of deep beams, with a discharge arch interesting most of the stone's volume and a quasi-uniform traction along the fiber opposite to the arch.

To support this description, in Fig. 2 we show the von Mises stress map in the vertical cross section of a single Abeille's flat vault ashlar with ideal contacts and load. The computation was performed using the model and assumptions that will be presented later in this paper to study the whole vault. The dimensions of the ashlar are given in the following table.

Maximum length	0.88 m
Maximum width	0.44 m
Height	0.20 m
Inclination of the faces on the vertical plane	$\pm\pi/4$ rad

The bending resistance of stones under such condition is sufficiently high for no records of tensile fracture in experiments on Abeille's vaults to exist.

2. Geometry

We focus on the particular case of spherical domes and Abeille's bonding, calling upon the automatic procedure presented in Brocato and Mondardini (2010), with some additions. Starting from a set of independent variables that define the bonding and geometry of a vault, and from the necessary physical information on materials and loads, the procedure performs a finite element structural analysis of the vault. The outcome of this analysis is then red in terms of a few parameters related to the structural performance of that vault. The search for the optimum is then made comparing candidate vaults.

The procedure was implemented using Wolfram Mathematica for the geometrical computations and visualizations and Cast3M (a general purpose finite element computer code developed by the French Atomic Energy Commission CEA), for the mechanical computations.

The geometry of the dome is defined starting from the choice of a geodesic sphere and applying to the edges of this polyhedron a transformation that creates a net having the interweaving property of a nexorade. The edges of this net are assumed to support the axes of the ashlars, which are then completely defined checking their contacts with the neighbors.

A geodesic sphere is a polyhedron whose vertices lay on the surface of a sphere and edges lay into planes that contain the center of the sphere (Kenner, 1976). If any such polyhedron can be chosen to start defining an Abeille's dome according to our procedure (Brocato and Mondardini, 2011), we focus here on domes obtained starting from an icosahedron: a spherical mesh is obtained projecting the edges of this polyhedron from the center of the sphere to its surface; the result is then refined by triangulation to get denser meshes until the wanted density is reached (Brocato and Mondardini, 2010).

As quoted above, starting from the geodesic sphere, a procedure expedient for the design of nexorades is called to transform its

edges. A nexorade is a structure made of 'nexors', a beam often having four simple connections, two at its ends to be supported and two at intermediate points to bear other nexors. The elementary arrangement of nexors in a nexorade is called a 'fan'. Though not interesting here, nexors with more or less than four connections can be also considered.

As already discussed, Abeille's flat vault bond is closely related to the sketch of Serlio's: both of them provided a solution for the problem of covering a space with elements shorter than the span, based on a square tiling. Serlio's can be seen as a nexorade made of flat four nexors fans; consequently the same can be said of Abeille's and methods useful for the general design of nexorades can be hired for our purposes.

Hence a method applicable for the design of nexorades is applied (Baverel, 2000; Baverel et al., 2000; Baverel and Nooshin, 2007): given any regular or semi-regular polyhedron, the nexor's axes of the corresponding nexorade can be obtained by rotating each edge of the polyhedron about its mid point of the same angle about an axis radiating from the center of the solid.

In our procedure, for all edges of the geodesic sphere, the mid point is identified and the normal to the sphere through this point is taken; then a rotation of an angle α (an amplitude defined by the designer between 0 and $\pi/2$, ends excluded) about this normal is applied to the edge to obtain the nexors. We call α the *chirality angle* because it rules the chiral morphology of the fabric. Fig. 3 shows the result of the step for an hemisphere.

The operation creates a list of three local coordinates axes per nexor, taking the nexor's axis t_i, the normal to the sphere in the mid point of the nexor n_i, and their vector product $t_i \times n_i = m_i$).

Furthermore, a topological information must be recovered, to decide which nexors cross each other, a task that is accomplished checking the distances between the end points of the segments representing the nexor's axes to decide, for all nexors, which nexor lays right at the left-hand side and which right at the right-hand side of it (left and right being uniquely defined with respect to the local axes, standing as n_i and looking in the direction of t_i).

The stereotomy of ashlars having such nexors as axes must then be defined. To begin with, the base trapezium, an isosceles one, is defined through the following parameters: b, the height measured along n_i, a_0, the length of the mid-segment measured along m_i, and φ, the angle of the legs on the normal direction n_i; the two bases are $a_1 = a_0 - b\tan\varphi$ and $a_2 = a_0 + b\tan\varphi$, with the axis t_i passing through the mid point of the mid segment of the trapezium (Fig. 4).

We call φ the *splice angle* to emphasize its importance in the bond ruling the inclination of contact surfaces on the vault's ideal spherical surface. For $\varphi \to 0$ there is no splice effect in the contact and the vault's resistance relies mostly—if not entirely—on thrust;

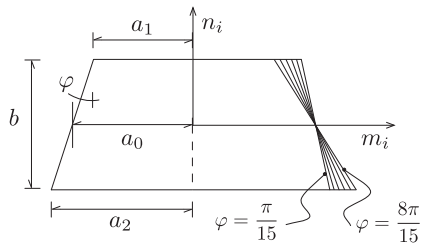

Fig. 4. Cross section of the ashlars. The legs of all trapezia considered in the analyses are drawn on the right hand side of the picture.

for large enough values of φ (whose upper limit $\pi/2$ is geometrically meaningless) a stacking effect would take place and the levery mechanism eventually dominate over the inverted catenary one. The splice effect appears in between as a combination of thrust and stack made possible by friction.

This angle could also be named after the planes it defines, called "*coupes*" in French treatises on stereotomy dealing with flat arches (see e.g. Douliot, 1825), but *layer*, the corresponding English term, does not seem appropriate here.

Notice that a possible change of sign of φ corresponds, mechanically, to the passage from end-supported stones bearing their neighbors between supports to center-supported stones bearing their neighbors as cantilevers and, from the esthetic point of view, from a smooth to a carved intrados. The mechanical consequence of such a change are not further explored in this paper.

For the examples that will follow we have taken $b = 0.0857r$, and $a_0 = 0.07875r$, where $r = 5$ m is the radius of the sphere, while variations of φ where explored. Vaults of spherical shape, but spanning less than the hemisphere can also be considered, choosing the spherical cap cut by the plane at a distance ζr from the center of the sphere ($0 \leqslant \zeta < 1$). In particular we have taken $\zeta = 0.75$ and thus a span $s = 1.3229r$.

Given a cross section and an axis, the shape of all stones must then be defined in such a way that they all fit with their neighbors. A tentative set of shapes is for this purpose generated taking right prisms having the same trapezoidal base and the height along the nexor direction t_i. Knowledge of the topological relation between nexors can then be used to compute the intersections between the parallel edges of each such prism and the surfaces identified by one side of the neighboring prism right at its left-hand or right-hand. Notice that, due to the curvature of the approached spherical surface, these edges do not necessarily reach the faces of the neighboring prism and will, in this case, be cut at the point where they cross the plane of that face. The prism's bases are then

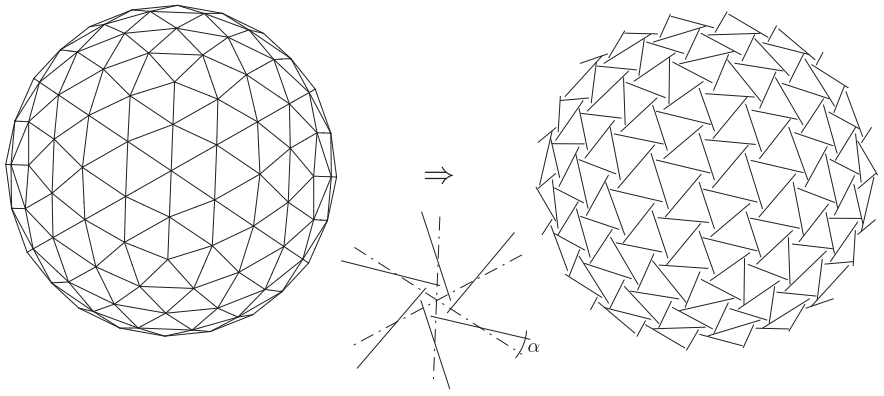

Fig. 3. Nexorade sketch (right) obtained from half a geodesic sphere (left) rotating edges of a chirality angle $\alpha = \pi/10$ about the normal to the surface of the sphere passing by their mid point.

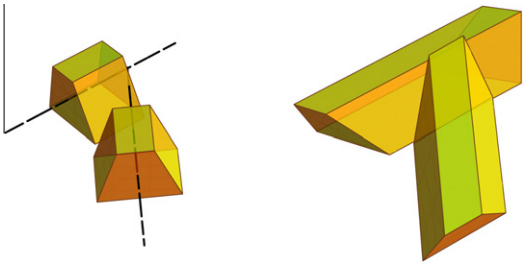

Fig. 5. Shaping of the ashlars to make them in contact with each other. The the left-hand side of the picture shows two right prisms with their height along nexors (nexors are denoted by a dashed segment) that are transformed into those on the right. Ashlars shaped as shown at the right-hand side of the picture make up together a vault of the type we name A.

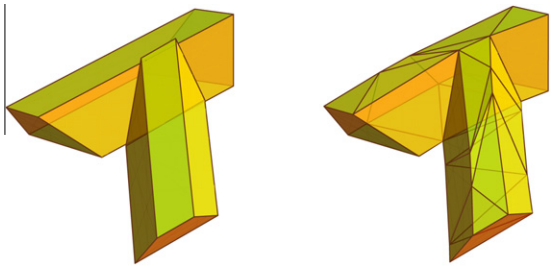

Fig. 6. Reshaping of the ashlars to give the intrados and extrados of the vault the shape of polyhedra with vertices on the surface of a sphere. The prismatic ashlars on the left-hand side of the picture are transformed into those on the right. The latter make together up a vault of the type B.

cut away at the appropriate angle to get the proper contact conditions with its neighbors. Fig. 5 shows the procedure for a couple of nexors.

In addition to these intersections defining the ashlar's bases, the ideal print of each of them on the lateral surface of adjacent stones is computed, a useful piece of information when assembling the vault.

The resulting dome is made of ashlars that are all prisms with the same cross section and differ only for the inclination of their bases (a striking asset for the economy of the construction). In such a dome the intrados and extrados surfaces display jumps at all nexor's contacts.

If a smoother appearance is sought, a modification of the vault's appearance, if not necessarily of the structural performances, can be obtained changing the shape of stones in such a way that all vertices at the extrados lay on the same spherical surface and all vertices at the intrados lay on another concentric spherical surface.

This result can be obtained keeping in their plane all faces where a contact between ashlars occurs, but changing their shape in this plane to make the vault's intrados and extrados as close to spherical surfaces as needed. In this way the intrados and extrados lateral faces of the stones will no more be planar surfaces, but out of plane polyhedral or curved surfaces; ashlars will be nonconvex polyhedra.

In particular we will take into account the case when the vault's intrados and extrados are shaped as convex polyhedra. We will denote by A vaults of the first type (prismatic ashlars) and by B those of the second type (nonconvex polyhedral ashlars).

Fig. 6 shows a reshaping of this kind (different polyhedral shapes can be chosen to answer to the need); it must be noticed

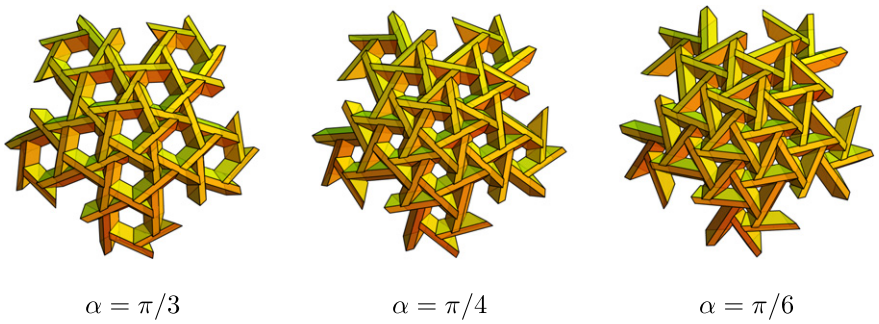

Fig. 7. View of the pattern on the extrados of spherical Abeille's bonds obtained for different values of the chirality angle α.

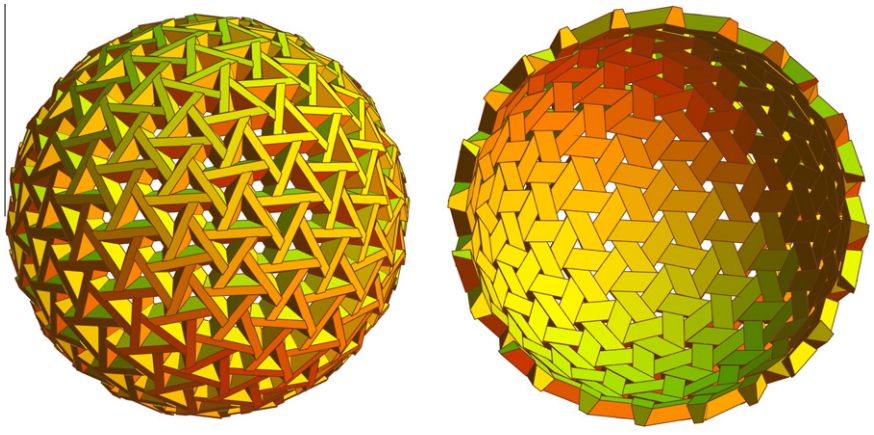

Fig. 8. Extrados (left) and intrados (right) of an Abeille's hemispherical dome with prismatic ashlars (type A).

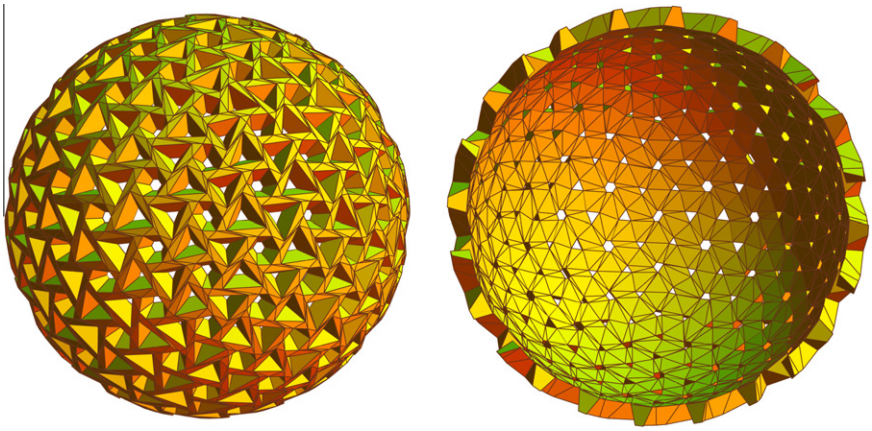

Fig. 9. Extrados (left) and intrados (right) of an Abeille's hemispherical dome with the intrados and the extrados reshaped as polyhedra with vertices on the surface of a sphere (type B).

that other procedures can be followed to get the wanted result that do not preserve the flatness of contacts.

The procedure described above is entirely automatic. All parameters ruling the geometry of the vault can be chosen by the designer to enhance the performance and esthetics of the construction. Fig. 7 shows for instance three of the possible patterns (with prismatic ashlars) that can be obtained by different values of the chirality angle α.

Fig. 8 shows the view from the extrados and the intrados of one of the possible resulting Abeille's dome of type A and Fig. 9 shows a case of type B.

3. Mechanical analyses

3.1. Choice of the model

To compare vaults on a mechanical basis we need a model of them. Many possibilities exist to define such a model and the choice of the most appropriate one in the present circumstances can be driven by the following considerations.

Structures of the kind we are studying are made of solid blocks of stone (the ashlars) separated by thin interfaces filled with mortar (the joints). Interfaces play a paramount role in the actual behavior of the system and models not including them—at least loosely—are known to be poorly predictive, unless the analysis of a very reduced class of phenomena is sought. Hence the alternatives:

- Look at the ashlars and the joints as deformable solids of different nature, perhaps displaying nonlinear behaviors and even displacement jumps across the joints, and make a homogeneous equivalent model of the heterogeneous system they compose.
- Consider masonry as an ideal no-tension material or as a material with smeared cracks (usually seen as an homogeneous one) and perform non-linear analyses.
- Neglect the deformability of the ashlars and model the system as a discrete set, with displacements occurring only (or mainly) at the interfaces between rigid (or roughly deformable) blocks.
- Make a fully heterogeneous nonlinear model of the structure, with deformable—conceivably linear elastic—solid blocks to represent the ashlars and deformable nonlinear interfaces to represent the joints.

A benchmark of three different models of masonry structures and a comparison of numerical and experimental results is given by Giordano et al. (2002). The models were: a finite element one with discontinuities obtained with Cast3M under assumptions similar to those we are going to take, a finite element continuous one made with ABAQUS considering a homogeneous material with smeared cracks, and a discrete elements one made with UDEC (Universal Distinct Element Code). The three models are shown to be in good agreement with the experiments. The main weakness of the first is, according to the authors, related to the need of remeshing in case of large displacements; the second fails predicting cyclic behaviors, and the third needed—at that time—further developments to take deformable blocks into account.

The results of a comparative study of different models, made to support the decision on the modeling strategy to adopt, is given in Figs. 10 and 11. These load–deflection curves are computed for a loading that will be presented later on in this section and are shown here to justify our choice of the model.

The first and second approach in the previous list are mostly appropriate for brickworks, where the characteristic size of the heterogeneities is much smaller than that of the structure. For this reason we will follow neither of them in this paper. A review of homogenization approaches proposed for masonry structures is given by Lourenço et al. (2007).

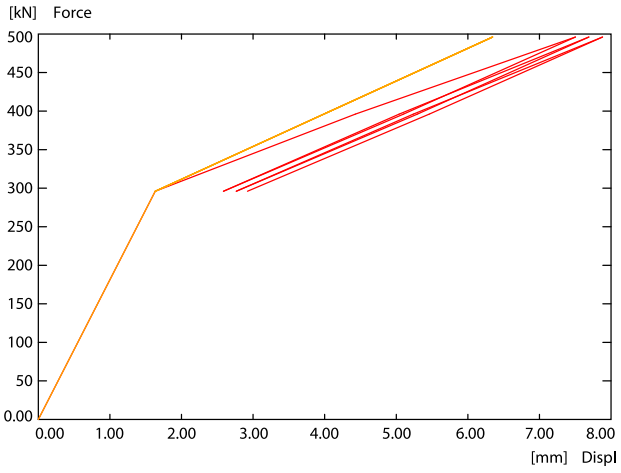

Fig. 10. Comparison of the load–deflection curves for the vault $\alpha = \frac{3\pi}{20}$ and $\varphi = \frac{2\pi}{15}$ obtained through a linear elastic continuous model (orange) and the nonlinear model used to obtain all other results in this paper (red). The Young modulus of the linear model was taken to fit with the first branch of the non-linear result, i.e. at a value about 1/55 of the Young modulus of the stone considered in the non-linear numerical analyses. (For interpretation of the references to color in this figure legend, the reader is referred to the web version of this article.)

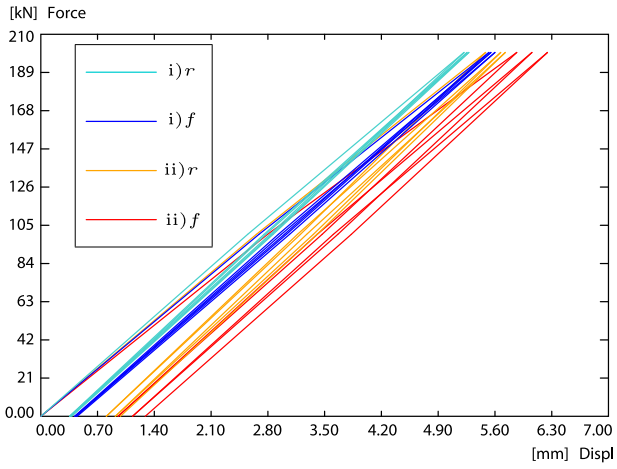

Fig. 11. Comparison of the load–deflection curves for the vault (i) $\alpha = \frac{23\pi}{120}$ and $\varphi = \frac{\pi}{15}$ versus (ii) $\alpha = \frac{3\pi}{20}$ and $\varphi = \frac{2\pi}{15}$, obtained through a rigid ashlar model (r) and the nonlinear model used to obtain all other results in this paper (f). The choice of these two vaults is motivated by the fact, explained into further detail in a subsequent part of this paper, that they display the minimum and maximum residual displacement after the selected loading tests.

Results obtained for our structure through a linear homogeneous and a non-linear heterogeneous model are compared in Fig. 10 to support the choice of the latter. In this figure the load–displacement curve of a linear elastic continuous vault (no joints) is compared with that of the same vault obtained through the non-linear model chosen for the other developments presented in this paper. The vault corresponds to the taken $\alpha = \frac{3\pi}{20}$ and $\varphi = \frac{\pi}{15}$ and is of type A. Loading, boundary conditions and reference points for the measure of the deflection are those adopted for all the analyses that follow and will be presented in details later in this paper. The Young modulus of the equivalent homogeneous material included in the linear model was chosen fitting the first branch of the non-linear result: a value of 5.4 MPa was taken i.e. about 1/55 of the Young modulus of the stone considered in the non-linear numerical analyses.

The result indicates clearly that the geometry of joints is a paramount feature in the physical system and that a load-dependent homogeneous behavior is to be determined to mimic the system's evolution. A task (so far proposed for periodic or statistically homogeneous systems), per se, challenging in our case due to the spatial arrangement of heterogeneities based on a tessellation of the sphere and to the size of ashlars compared with that of the vault.

Rigid blocks discrete systems are often used in dynamics, when a simplified model of the contact interaction is expedient. In such models velocity jumps are expected when blocks collide with each other and the distribution of stresses, within blocks and at their contacts, are naturally indeterminate. The first issue is possibly tackled via a shock law and less a concern in our case, as we are not searching for an optimal dynamic response of the structure. Within the framework of Non-Smooth Contact Dynamics, Jean (1999) avoids the second issue analyzing numerically 144 (10 cm × 5 cm) elastic blocks with Mohr–Coulomb joints. In the same framework, with similar joints but rigid blocks, Rafiee et al. (2008) computed the response of arches to dynamic loadings. An elasto-plastic model of the contact interaction is used instead by El-Raheb (2010), proving effective for the seismic analysis of stone-walls staying on dry friction contacts. These results encourage the recourse to similar models in our case.

A comparison of results obtained for structures of the kind we are studying considering rigid or deformable blocks, with equal interfaces, is shown in Fig. 11. The model with deformable blocks will be presented in the following part of this section, while the model with rigid blocks is simply obtained from it rising the Young modulus of the ashlars' material of three orders of magnitude. Loading, boundary conditions and the point where deflections are measured will be presented later in this paper. These results support the idea that the deformability of the ashlars do play a role in the system that cannot be neglected in quasi static conditions, which can be read not only—as obviously expected—by its effect on the deflection of the loaded structure, but also in the residual deformation after unloading.

The latter effect can be explained as a result of the influence of the deformability of the hyperstatic structure on the load descent path—leading to a distribution of the contact stresses among interfaces that depend on the different stiffnesses of the ashlars—an issue that is less a concern in a single arch or in a reasonably regular wall, the structural types that were studied in the quoted literature.

Whatever the preferred model for the structure, a limit analysis can be done. E.g. the path opened by Suquet (1983) can be followed to study the failure limit of periodic arrangements of heterogeneous rigid-plastic associated materials. Such analyses give no information on the structure's pre-failure behavior. Hence a limited interest in the present case toward approaches of this kind, as we wish to produce results for the design of new structures, whose performances are not only to be tested at the ultimate strength limit, but also during service.

3.2. Definition of the model

Taking into account the previous results and considerations, we decided modeling the vault as a discontinuous set of deformable ashlars in contact with each other through thin mortar layers and analyze it as an heterogeneous system by the finite element method.

For this purpose ad hoc programmed software interfaces export from Mathematica to Cast3M information on the local topology and coordinates of the vertices of each ashlar. All higher level geometric and topologic information is then re-build in the latter code. In particular, edges are built from vertices, faces from edges and volumes from faces, having thus each stone meshed into a block of finite tetrahedral elements.

Contacts occurring between such blocks must then be detected and all interfaces identified by means of a proximity criterion. Then a mesh adjustment is needed because, on these interfaces, nodes on the boundary of one block do not necessarily correspond, one to one, to nodes of the other block's boundary, which eventually arises incompatibility issues in calculations. Hence it is necessary to transform incompatible couples, that are possibly created when blocks are meshed independently of each other, into compatible ones.

For this purpose, using the Cast3m's 'CBLO' operator (Pegon, 1999), each edge of each block's mesh is inspected; if a master node of another block is found closer to this segment than a gap gauge, the node is duplicated and added to the mesh of the current block. A similar procedure is performed for all parts of the mesh. At the end of it, all surfaces facing each other with a gap thinner than the gauge, have master nodes corresponding one to one.

Stone blocks are then modeled as linear elastic solids (different mechanical behaviors being applicable if needed), with the usual parameters:

ρ_s	Density
E_s	Young modulus
v_s	Poisson ratio

The material characteristics of stone were obtained from laboratory tests performed on tender limestone with miliole (the so called *royal bench*) from Noyant, France. The Young modulus E_s was estimated starting from a measured sound speed $v = 2500$ m/s as

$$E_s = 3(1 - \nu_s)\rho_s v^2.$$

The density ρ_s was directly measured and the Poisson ratio ν_s was taken according to standard values for the kind of stone.

Interfaces are modeled as joints with Mohr–Coulomb behavior by means of the 'GENJ' operator (Pegon et al., 2001), implemented in the standard release of Cast3m: compression forces and tangential forces limited by friction can be exchanged across them; stones can separate and/or glide on each other under the action of contact forces. This model is defined by the parameters:

ρ_m	Density
K_n	Compression elastic modulus
K_s	Shear elastic modulus
c	Cohesion
ϕ	Friction angle

The joint behaves elastically inside the Mohr–Coulomb domain defined in terms of normal stress σ and shear stress τ by

$$|\tau| \leqslant (c - \sigma)\tan\phi$$

(assuming positive tensile normal stresses). An associated plastic flow rule defined by a dilatancy angle equal to the friction angle ϕ is adopted when the stress vector lies on the surface of this domain, i.e., in terms of gliding rate γ and opening rate δ:

$$\delta = |\gamma|\tan\phi.$$

The perfect unilateral contact is one obeying the Signorini condition: there is a contact gap that can be closed or open but interpenetration is forbidden, a necessarily compressive reaction exists if and only if the gap is closed. This unilateral constraint is treated in Cast3m through a penalization method where K_n plays the role of a multiplier; hence a possible overlap of the contact faces in numerical results.

The mortar's density ρ_m and Poisson ratio ν_m were set through an experience-based assessment. The mortar's elastic modulus E_m was obtained from a full scale test on an arch made of the above mentioned stone with *Fermaflex* mortar joints. *Fermaflex* is the brand of a bi-component adhesive mortar with synthetic latex in aqueous emulsion and a cement, sand, and cellulosics, based powder. The value of the elastic modulus of the joints was taken fitting with measures the computed value of the maximum deflection, the simulation being done through the same kind of finite element model presented here.

The parameters needed in the finite element model were computed from the above mentioned material parameters (t the joint's thickness):

$$K_n = \frac{E_m(1-\nu_m)}{t(1-\nu_m-2\nu_m^2)}; \quad K_s = \frac{E_m}{2t(1+\nu_m)}.$$

The material parameters that were used for calculations are listed in the following table.

Ashlars	Density	ρ_s	2000 kg/m^3
	Young modulus	E_s	27.375 GPa
	Poisson ratio	ν_s	0.27
Joints	Thickness	t	5 mm
	Density	ρ_m	2500 kg/m^3
	Young modulus	E_m	3.0 MPa
	Poisson ratio	ν_m	0
	Cohesion	c	0
	Friction angle	ϕ	π/4 rad

The boundary conditions have been defined exporting from Mathematica to Cast3M the information of the outer faces of the stones of the outer ring. These faces were considered in calculations resting on Mohr–Coulomb contacts on a rigid confinement ring.

The considered loading actions were the self-weight plus a variable load. The former depends on the geometry and was imposed gradually as when striking a centering. The latter was applied as a evenly distributed force per unit surface in the vertical direction on top of the vault, precisely on the upper faces of the six ashlars

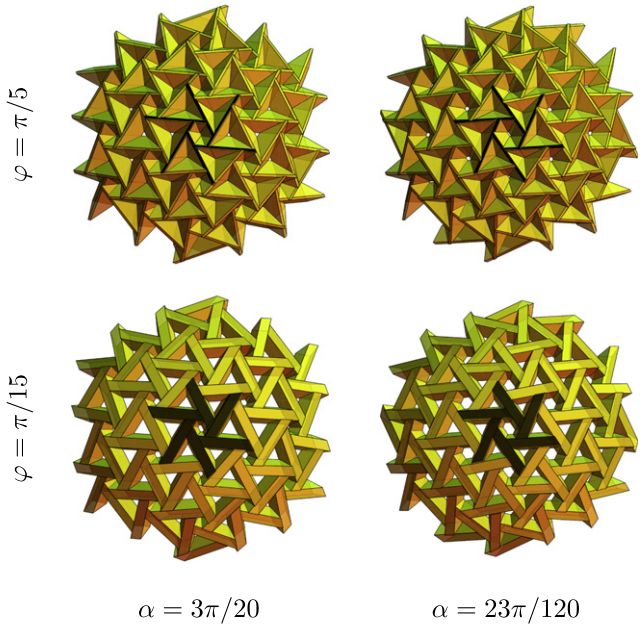

Fig. 12. View of the extrados of some of the explored A vaults for different values of the chirality angle α and of the splice (positive) angle φ; $\zeta = 0.75$. The dark tint indicates the area where a vertical variable load is applied in addition to the self weight.

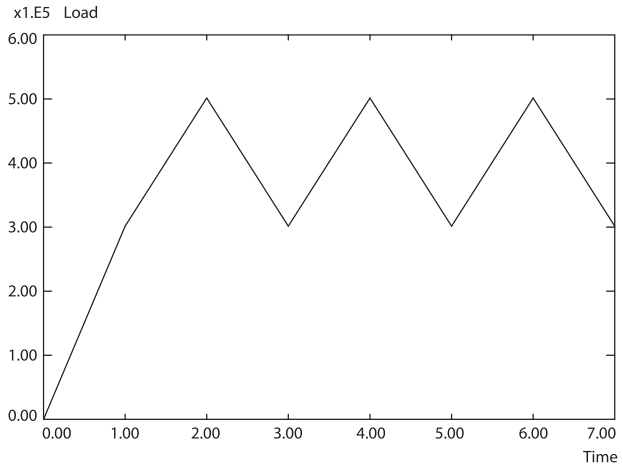

Fig. 13. Loading is given by the self-weight (depending on the geometry) plus a vertical distributed force whose resultant oscillates between 0 and 200 kN. The resultant of both fields [10^5 N] is plotted here versus a fictitious time.

closer to the top, oscillating quasi-statically with a sawtooth shape history and a resultant between 0 and 200 kN, during three charge–discharge cycles starting when the self-weight was fully applied (see Figs. 12 and 13). Notice that the resultant of the variable load was imposed, instead than the average pressure, to make results obtained with vaults of different shape comparable.

4. Analysis

As already mentioned, we restrict attention on vaults shaped as a spherical cap. All geometric parameters but two are fixed in the analysis to the values given in Section 2. Hence a two parameters family of vaults is studied, taking the chirality angle α (rotation of the nexors about the normal to the sphere passing through their midpoint) in a list of length 6:

$$\alpha \in \left(\frac{3\pi}{20}, \frac{19\pi}{120}, \frac{\pi}{6}, \frac{7\pi}{40}, \frac{11\pi}{60}, \frac{23\pi}{120}\right)$$

(i.e., angles starting from $\frac{3\pi}{20}$ with step $\frac{\pi}{120}$) and the splice angle φ (inclination of the ashlar's nonparallel faces with respect to the meridian plane containing the ashlar's longitudinal axis) in a list of length 6:

$$\varphi \in \left(\frac{\pi}{15}, \frac{4\pi}{45}, \frac{\pi}{9}, \frac{2\pi}{15}, \frac{7\pi}{45}, \frac{8\pi}{45}\right)$$

(i.e., from $\frac{\pi}{15}$ with step $\frac{\pi}{45}$).

The choice of the two ranges is dictated by geometry: values of the chirality angle α closer to 0 or to $\frac{\pi}{2}$ generate fans of nexors that have their axes converging too close to a single point for the nexorade scheme to apply effectively (i.e. these axes are too close to the edges of an icosahedron when $\alpha \to 0$ or of a dodecahedron when $\alpha \to \frac{\pi}{2}$ for the load path in the structure to be not one of a geodesic dome); the two limits correspond in fact to a lack of chirality. Values of the splice angle φ closer to 0 make ashlars touch each others on surfaces that are almost orthogonal to the vault's middle sphere, thus reducing the stacking timber effect proper of Abeille's bond; larger values of φ than the considered ones give rise to contacts along the lateral faces of the ashlars (and the necessary geometric modification of their shape to avoid interpenetrations) that are not consistent with the studied static system, as ashlars would tend to transmit forces more as elements of a shell than as beams.

The analysis consists in running numerical tests through the family and comparing computational outputs. Further details on the procedure will be explained in the following part of this section.

The test was made on vaults of type A and B, but the two groups must be analyzed together to get a complete view. In fact, due to geometric oddnesses arising for some couples of the parameters α and φ and hindering the finite element meshing, not all vaults in the family A and B were actually tested numerically. The alluded oddnesses are due, in type A vaults, to the angular mismatch between edges of different ashlars at contact that, belonging to the same contact plane, do not lay on the same plane on the intrados or on the extrados; consequently very slender triangles must sometimes be cut on the contact faces to discretize them compatibly, thus demanding too high mesh densities for the numerical modeling.

On the other hand, computations for two vaults of type B were not performed because in such cases the rules introduced to define type B ashlars produce solids whose faces intersect with each others. Eliminating the mismatch would lead to the definition of a third type of vault, which we considered not worth studying in this paper.

The table below shows all studied cases, labeled 'A' and/or 'B' according to the type of vault that was tested.

φ \ α	$\frac{3\pi}{20}$	$\frac{19\pi}{120}$	$\frac{\pi}{6}$	$\frac{7\pi}{40}$	$\frac{11\pi}{60}$	$\frac{23\pi}{120}$
$\frac{8\pi}{45}$	B	–	B	B	A	B
$\frac{7\pi}{45}$	B	A B	A B	A B	B	A B
$\frac{2\pi}{15}$	A B	A B	B	B	A B	A B
$\frac{\pi}{9}$	A B	B	A B	A B	A B	A B
$\frac{4\pi}{45}$	B	A B	A B	A B	A B	A B
$\frac{\pi}{15}$	A B	A B	A B	A B	A B	A B

Numerical tests where run to evaluate the optimal bond under mechanical criteria. Vaults where compared with respect to the following pieces of information.

1. Total weight of the structure (lighter vaults being better candidates for an overall economy of the construction, see Fig. 14).
2. Maximum thrust (i.e. horizontal force in the radial direction) exerted by a single ashlar of the outer layer on the confinement ring at the springing contacts (smaller values corresponding to structures preferable with respect to the load descent, see Fig. 15).
3. Maximum deflection under self-weight (the information is irrelevant in itself, but useful to extract the active deflection, see Fig. 16). (see Fig. 17)
4. Maximum total deflection under the fist loading step (this deflection is considered as a measure of the structural stiffness before consolidation, see Fig. 14).
5. Maximum residual deflection after consolidating the structure by the quoted series of loading–unloading cycles (this deflection informs on the sensibility of the structure to consolidation, see Fig. 18).
6. Maximum cumulated gliding on contacts after these cycles (smaller values indicating better structures, see Fig. 19).
7. Applied force vs maximum deflection curves under live loads (shifted to clear all information on the self weight borne by the vault and the related deflection, see figures from Figs. 20–31).

Deflections mentioned above and given also in Figs. 10 and 11 were all measured as the vertical displacement of the highest point of the vault.

The lightest structure is obtained for $\alpha = \frac{19\pi}{120}$ and $\varphi = \frac{7\pi}{45}$; generally, weight decreases increasing φ. A similar tendency is observed

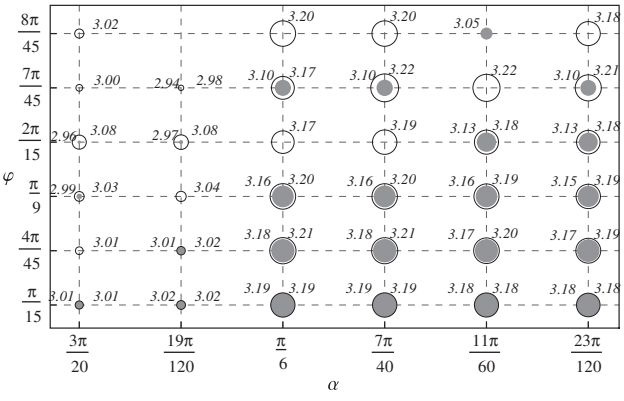

Fig. 14. Bubble diagram of the total weight of the vault [10^5 N] for different values of the chirality angle α and the splice angle φ. The radius of bubbles is taken as an affine function of the computed, labeled, value. Gray disks denote results for vaults of type A; the corresponding numerical values are written at their left. Empty disks within a black circle refer to type B vaults; numerical values are at their right. The empty location corresponds to the vault that was not tested numerically.

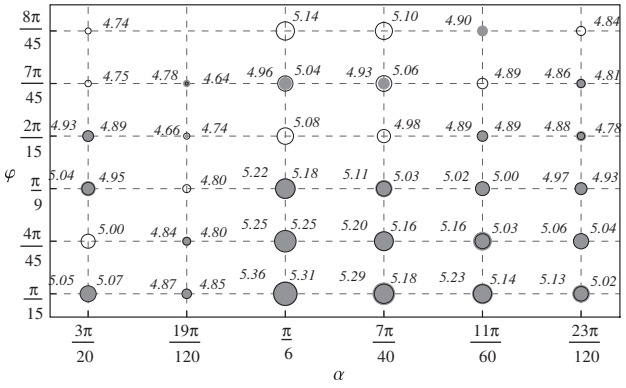

Fig. 15. Bubble diagram of the maximum local thrust [10^4 N] at a springing joint under self weight for different values of α and φ. Symbols are explained in the caption of Fig. 14.

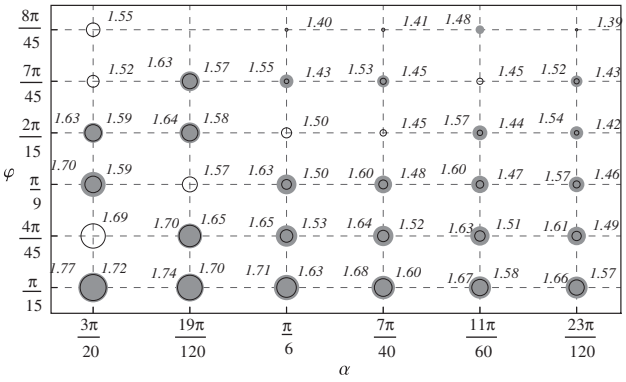

Fig. 16. Bubble diagram of the maximum vertical deflection [mm] under self weight for different values of α and φ. Symbols are explained in the caption of Fig. 14.

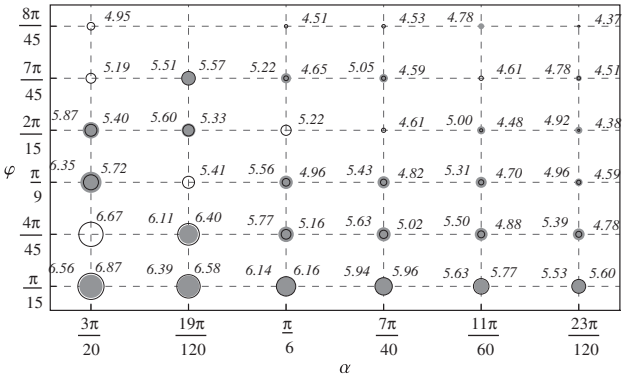

Fig. 17. Bubble diagram of the maximum vertical elastic deflection [mm] under variable and dead load for different values of α and φ. Symbols are explained in the caption of Fig. 14.

for the maximum thrust, where a maximum for $\alpha = \frac{\pi}{6}$ is also observed, with $\alpha = \frac{19\pi}{120}$ and $\varphi = \frac{2\pi}{15}$ for A vaults and $\varphi = \frac{7\pi}{45}$ for B vaults thrusting less than all the other cases. Notice that the ratio of the thrust on the weight is quasi uniform through the family (between 0.15 and 0.17), showing that all vaults perform similarly from the point of view of the arch effect.

Maximum vertical deflections under self weight or at the end of the first loading ramp are similarly affected by changes of the parameters: higher values of α and φ tend to give stiffer structures. The stiffest case is $\alpha = \frac{23\pi}{120}$ and $\varphi = \frac{8\pi}{45}$.

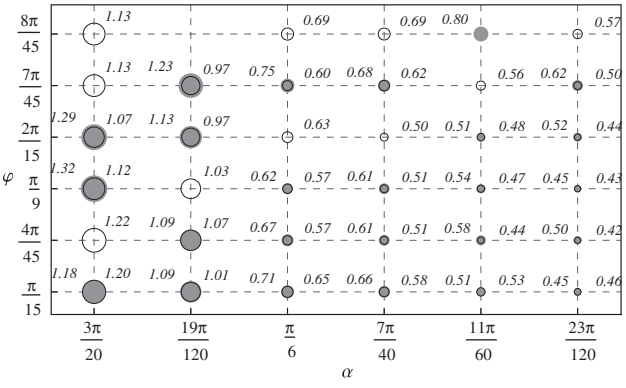

Fig. 18. Bubble diagram of the maximum vertical residual deflection [mm] after all loading–unloading considered cycles for different values of α and φ. Symbols are explained in the caption of Fig. 14.

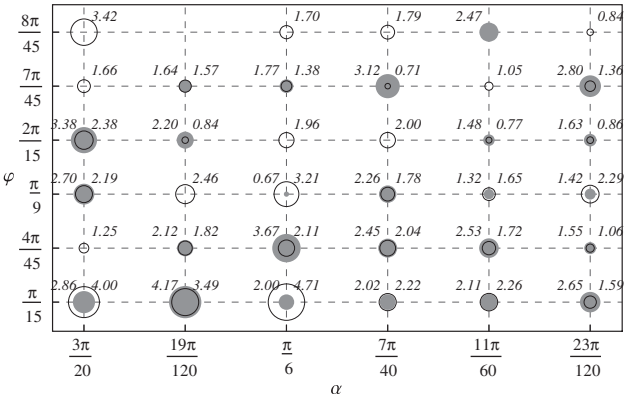

Fig. 19. Bubble diagram of the maximum cumulated plastic deformation [10^{-3}] at joints for different values of α and φ. Symbols are explained in the caption of Fig. 14.

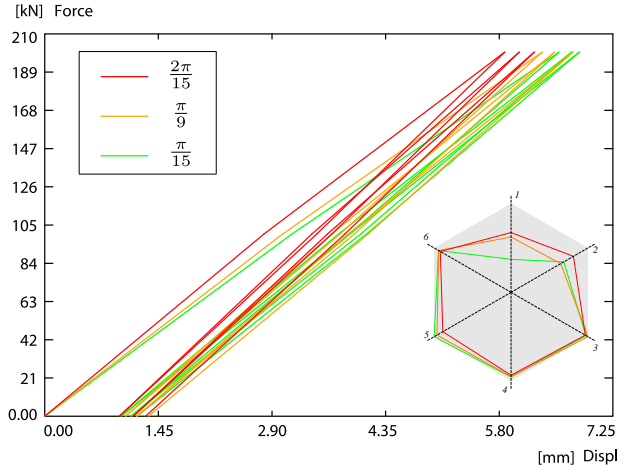

Fig. 20. Variable load vs deflection curves for a type A vault with chirality angle $\alpha = \frac{3\pi}{20}$, colored according to the indicated values of the splice angle $\varphi \in (\frac{\pi}{15}, \frac{\pi}{9}, \frac{2\pi}{15})$. The radar diagram in the gray hexagon has values on the axes that are the ratio between a given data for the given vault and the largest such value obtained for all vaults. Data are displayed as follows on the axes, turning clockwise from the top vertex: (1) increment of the residual deflection at the last loading step divided by the total residual deflection at the end of the last step, (2) maximum cumulated slip, (3) total residual deflection, (4) initial stiffness (increment of load for unit deflection at the first loading ramp) on final stiffness (the same, at the last ramp), (5) initial compliance (the reciprocal of the initial stiffness), (6) maximum side thrust. Unit values are at the vertices of the gray hexagon, zero at its center.

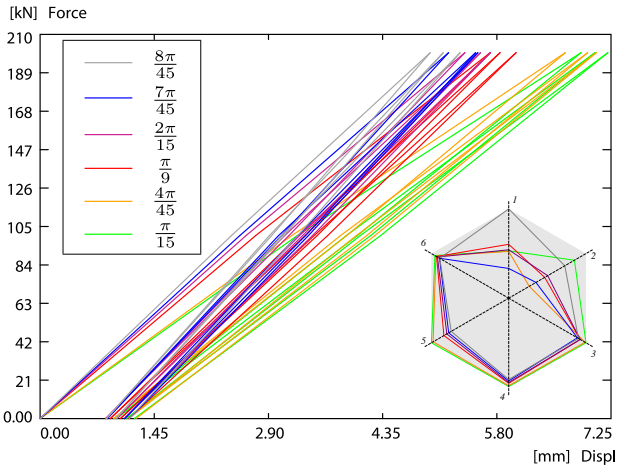

Fig. 21. Variable load vs deflection curves for a type B vault with $\alpha = \frac{3\pi}{20}$, colored according to the indicated values of $\varphi \in (\frac{\pi}{15}, \frac{4\pi}{45}, \frac{\pi}{9}, \frac{2\pi}{15}, \frac{7\pi}{45}, \frac{8\pi}{45})$. See Fig. 20 for the radar hexagonal diagram.

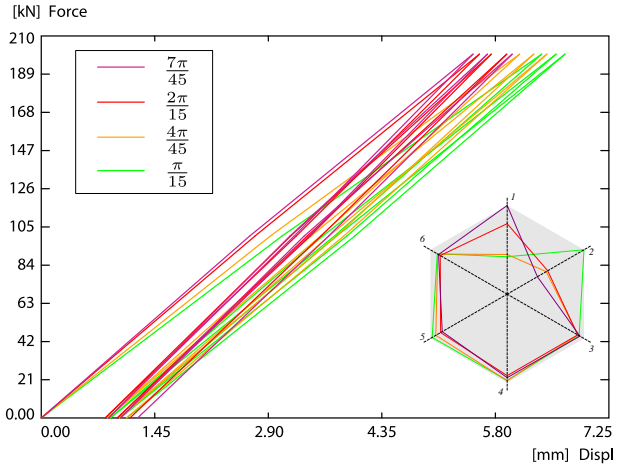

Fig. 22. Variable load vs deflection curves for a type A vault with $\alpha = \frac{19\pi}{120}$, colored according to the indicated values of $\varphi \in (\frac{\pi}{15}, \frac{4\pi}{45}, \frac{2\pi}{15}, \frac{7\pi}{45})$. See Fig. 20 for the radar hexagonal diagram.

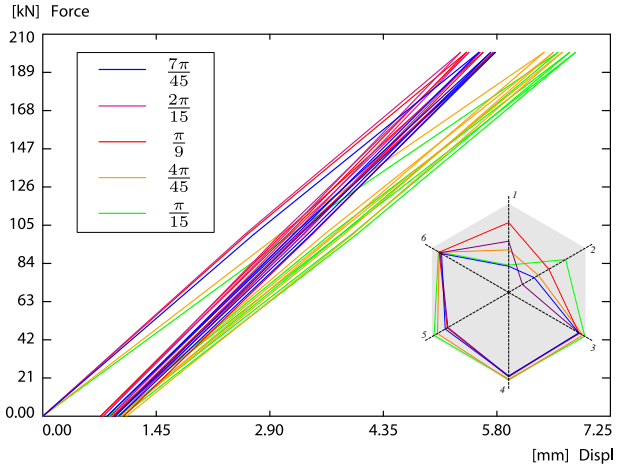

Fig. 23. Variable load vs deflection curves for a type B vault with $\alpha = \frac{19\pi}{120}$, colored according to the indicated values of $\varphi \in (\frac{\pi}{15}, \frac{4\pi}{45}, \frac{\pi}{9}, \frac{2\pi}{15}, \frac{7\pi}{45})$. See Fig. 20 for the radar hexagonal diagram.

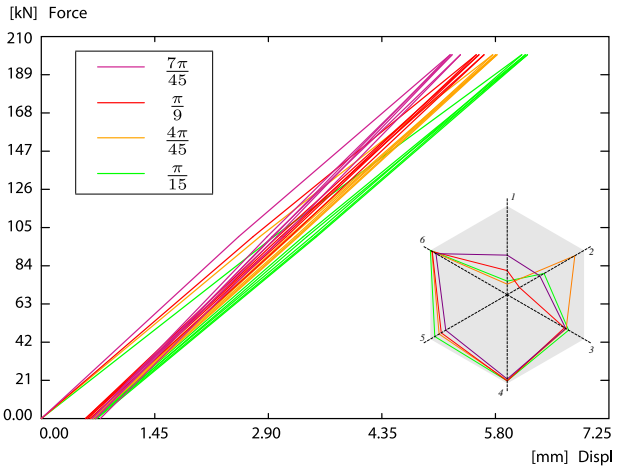

Fig. 24. Variable load vs deflection curves for a type A vault with $\alpha = \frac{\pi}{6}$, colored according to the indicated values of $\varphi \in (\frac{\pi}{15}, \frac{4\pi}{45}, \frac{\pi}{9}, \frac{7\pi}{45})$. See Fig. 20 for the radar hexagonal diagram.

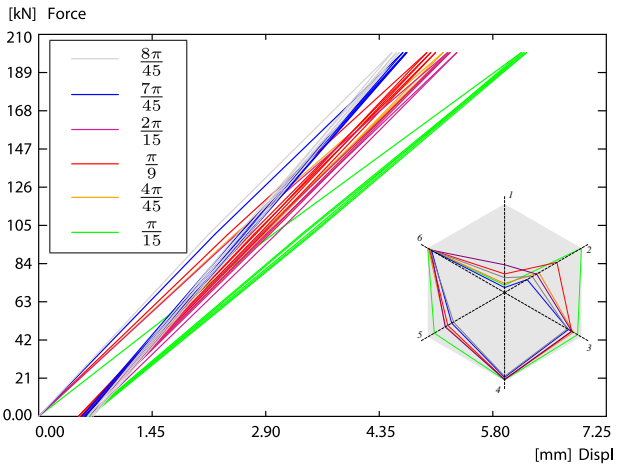

Fig. 25. Variable load vs deflection curves for a type B vault with $\alpha = \frac{\pi}{6}$, colored according to the indicated values of $\varphi \in (\frac{\pi}{15}, \frac{4\pi}{45}, \frac{\pi}{9}, \frac{2\pi}{15}, \frac{7\pi}{45}, \frac{8\pi}{45})$. See Fig. 20 for the radar hexagonal diagram.

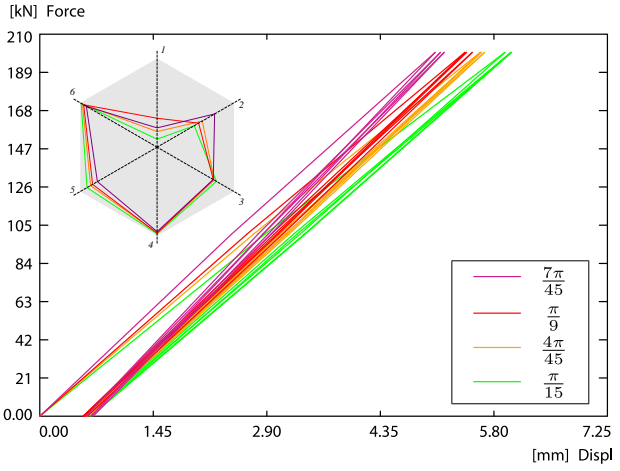

Fig. 26. Variable load vs deflection curves for a type A vault with $\alpha = \frac{7\pi}{40}$, colored according to the indicated values of $\varphi \in (\frac{\pi}{15}, \frac{4\pi}{45}, \frac{\pi}{9}, \frac{7\pi}{45})$. See Fig. 20 for the radar hexagonal diagram.

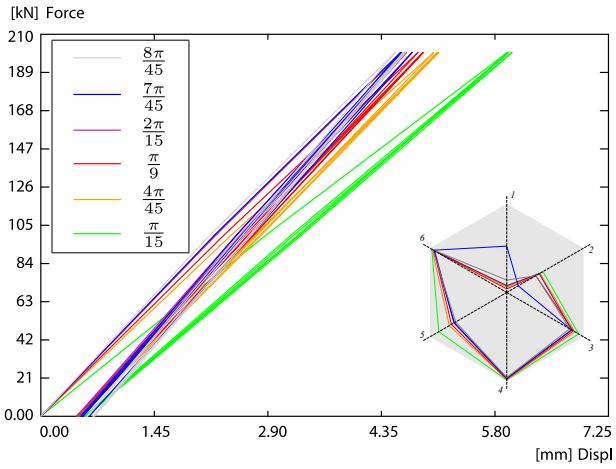

Fig. 27. Variable load vs deflection curves for a type B vault with $\alpha = \frac{7\pi}{40}$, colored according to the indicated values of $\varphi \in (\frac{\pi}{15}, \frac{4\pi}{45}, \frac{\pi}{9}, \frac{2\pi}{15}, \frac{7\pi}{45}, \frac{8\pi}{45})$. See Fig. 20 for the radar hexagonal diagram.

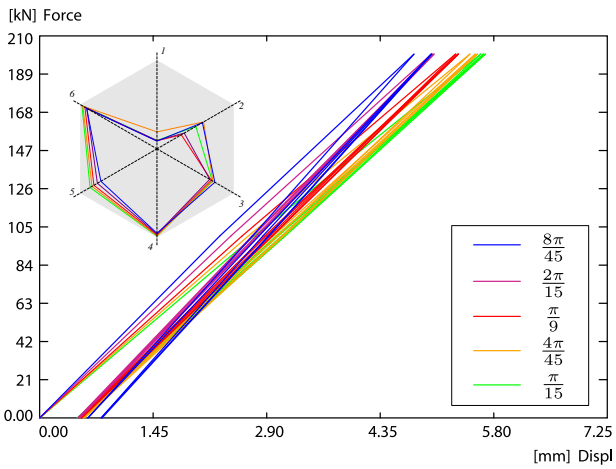

Fig. 28. Variable load vs deflection curves for a type A vault with $\alpha = \frac{11\pi}{60}$, colored according to the indicated values of $\varphi \in (\frac{\pi}{15}, \frac{4\pi}{45}, \frac{\pi}{9}, \frac{2\pi}{15}, \frac{8\pi}{45})$. See Fig. 20 for the radar hexagonal diagram.

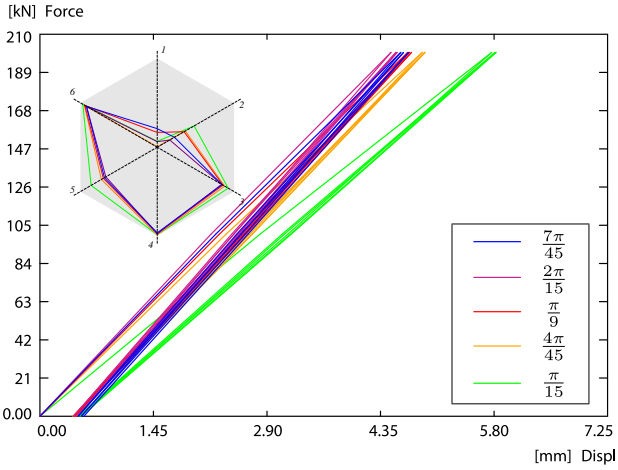

Fig. 29. Variable load vs deflection curves for a type B vault with $\alpha = \frac{11\pi}{60}$, colored according to the indicated values of $\varphi \in (\frac{\pi}{15}, \frac{4\pi}{45}, \frac{\pi}{9}, \frac{2\pi}{15}, \frac{7\pi}{45})$. See Fig. 20 for the radar hexagonal diagram.

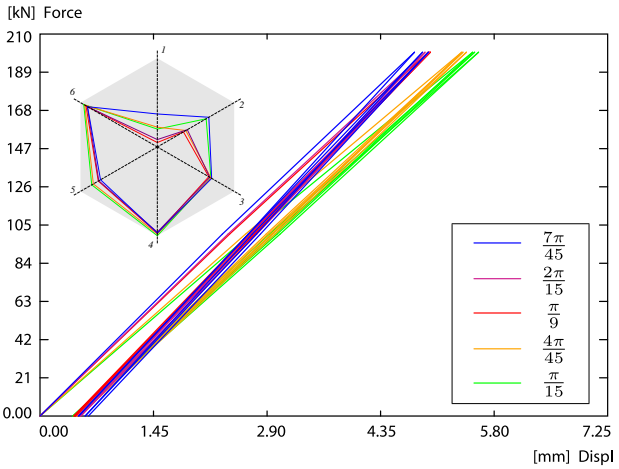

Fig. 30. Variable load vs deflection curves for a type A vault with $\alpha = \frac{23\pi}{120}$, colored according to the indicated values of $\varphi \in (\frac{\pi}{15}, \frac{4\pi}{45}, \frac{\pi}{9}, \frac{2\pi}{15}, \frac{7\pi}{45})$. See Fig. 20 for the radar hexagonal diagram.

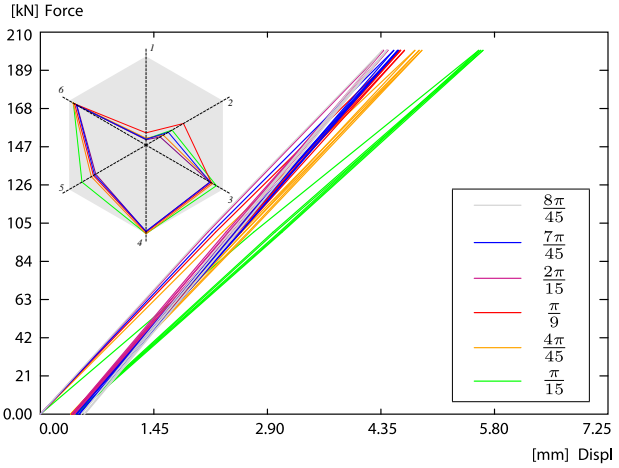

Fig. 31. Variable load vs deflection curves for a type B vault with $\alpha = \frac{23\pi}{120}$, colored according to the indicated values of $\varphi \in (\frac{\pi}{15}, \frac{4\pi}{45}, \frac{\pi}{9}, \frac{2\pi}{15}, \frac{7\pi}{45}, \frac{8\pi}{45})$. See Fig. 20 for the radar hexagonal diagram.

The behavior with respect to residual deflections is different: still, larger chirality angles α correspond to less yielding structures, but now the smaller the splice angle φ the lesser the computed deflection.

The cumulated plastic deformation at the joints has a pattern that suggests the existence of a locus of minima at values of φ between $\frac{4\pi}{45}$ and $\frac{2\pi}{15}$ or not far from them, though the sensibility to parameter α is much less clear in this case. The analysis of cumulated gliding is difficult because of the relatively small amount of such effect and because of the need of comparing local movements occurring in different structures. To build an objective criterion we have chosen to compare maxima regardless of the location where they occur, which entails that the function displayed in Fig. 19 is not necessarily continuous with respect to the parameters.

Figs. 20–30 show the load–deflection curves and radar diagrams that recapitulate synthetically all relevant results and compare them.

The load–deflection curves show that higher values of α tend to give structures that are stiffer when first loaded. On the other hand, smaller values of α result in vaults that tend to consolidate slower.

The following parameters are used to have a synthetic view of all analyzed outputs of the computations:

1. The increment of the residual deflection at the last loading step, if divided by the total residual deflection at the end of the last step, gives a measure of the consolidation process occurring during the loading–unloading cycles: if small it indicates a vault that has been almost totally consolidated (no more progression of the cumulated deflection). Aiming at a small value of this parameter is thus a good strategy to optimize the structure.
2. The maximum cumulated slip denotes a negative phenomenon as the vault drifts out its nominal geometry in an irreversible and uncontrollable manner: hence the smaller this output the better the vault.
3. Total residual deflection, as the previous variable, indicates a negative performance and its smallest value must be pursued.
4. The ratio between the initial overall stiffness of the vault, as measured by the increment of the applied load per unit computed deflection at the first loading ramp, and its final stiffness (evaluated through the same measure, but at the last ramp), which indicates the positive hardening of the structure when consolidating; the smallest value, corresponding to a structure stiffer at the end than at the beginning of the experiment, is to be considered as the indicator of the best performance.

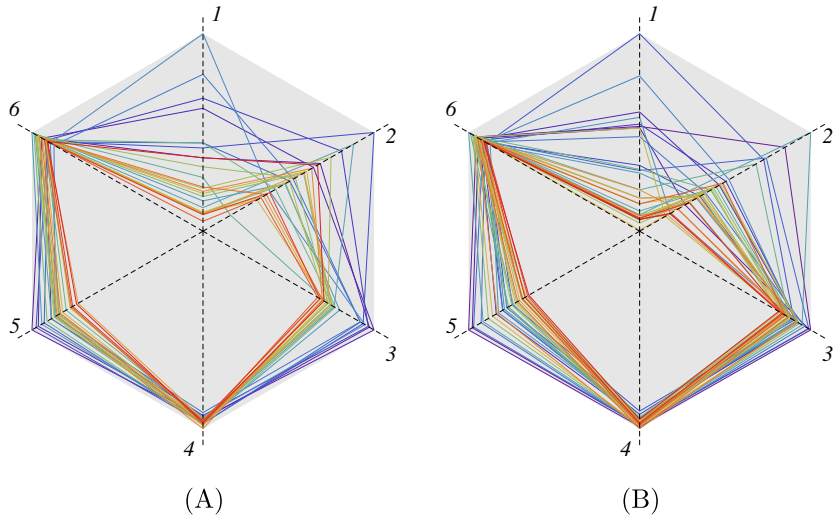

Fig. 32. Radar diagrams of all vaults superposed, type A on the left and B on the right. See Fig. 20 for the meaning of the radar axes. Polygons of different colors correspond to different vaults; the superposition of all diagrams has only a qualitative purpose, smaller groups of diagrams having been displayed in the previous figures. It should be noticed that the parameters on the axes 4 (bottom corner) and 6 (top-left corner) enter almost negligibly into play.

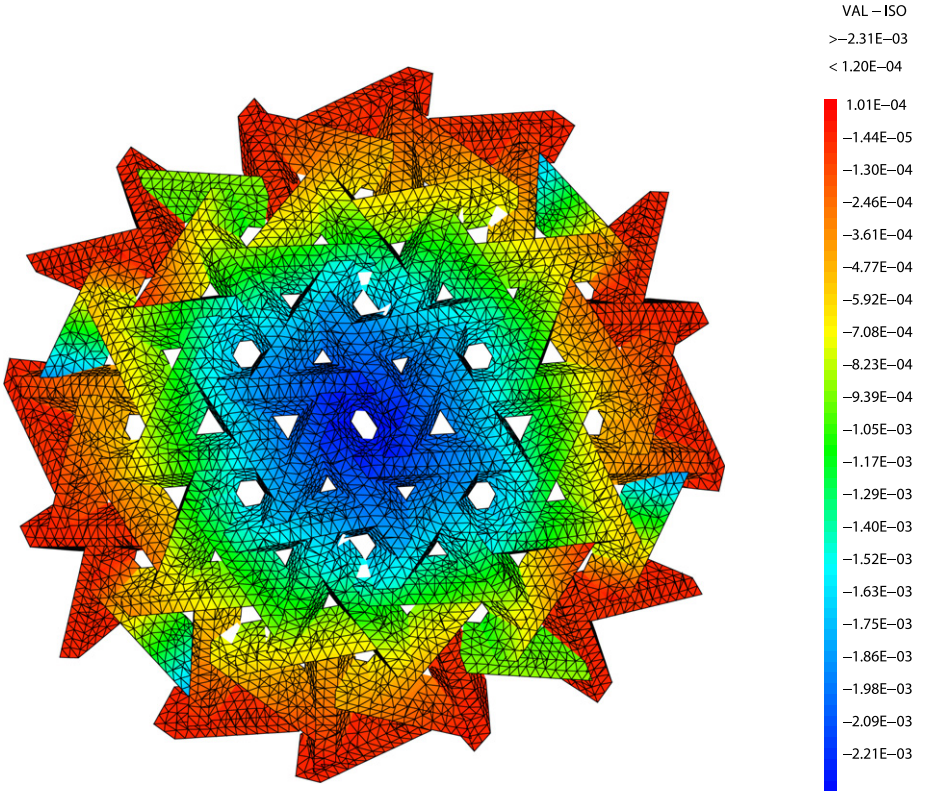

Fig. 33. The type A vault's vertical displacement under self-weight load for $\alpha = 23\pi/120$ and $\varphi = \pi/9$. Measures in [m].

5. The initial overall compliance of the structure, or the reciprocal of the initial stiffness as defined above, indicates, with a small value, a good structural behavior and a bad one with a high value (at least as far as stiffness is valuable in the particular case).
6. The maximum side thrust at the vault's springing is generally speaking the indicator of a need for a containment structure, whose stiffness and strength should be proportional to it; hence a minimal value for this maximum is to be sought.

As mentioned above, in Figs. 20–30 a radar diagram has been included in the gray hexagon to show synthetically the vaults' performance. The diagram has six axes were values are reported that are the ratio between a given data, for each vault, from the list above and the largest such value obtained for all vaults of the same family (A or B). Axes are thus scaled from 0 (at the center of the hexagon) to 1 (at the corners), with better performances closer to the center. Hence radar figures of smaller area tend to represent better performing structures.

All cases included, active deflections at the first loading ramp are between 4.5 mm and 6.5 mm for a live load resultant of 200 kN, i.e. an overall initial stiffness between 44 MN/m and 31 MN/m, with consolidation hardening all structures of about 15% of their initial stiffness.

It should also be noticed that consolidation does not stop progressing sensibly after the third ramp when $\alpha \leqslant \frac{19\pi}{120}$, contrary to what happens for higher values of α.

A rationale for the ponderation of the above introduced criteria need be set to decide on the optimal choice of parameters, a setting that depends on the particular case and thus remains undefined in a study as general as the present one.

An overall measure of the performance of the vault can be obtained as a weighted sum of the values given along the axes of the radar diagram. For equal weights this measure is proportional to the surface of the represented polygon; otherwise, the different weights can be accounted for scaling the six axes of the radar diagram differently before taking the measure of this surface. Within the scope of the present investigation, having no hints to set such weighting rules, a more refined measure of the structural performance than the one given by equal weights cannot be produced.

Observing Fig. 32, where all radar diagrams are superposed to get an overall—if qualitative—view, it must be noticed anyway that some of the performance parameters display small differences when changing vaults and thus have a minor effect on the radar polygon surface (see, e.g., axes 4 and 6 of the radar).

The choice of the optimal vault can thus be driven mainly by the following information: (axis 1) the increment of the residual deflection at the last loading step divided by the total residual deflection at the end of the last step and (axis 2) the maximum cumulated slip; in addition—with a lesser effect—also (axis 3) the total residual deflection and (axis 5) the initial compliance can contribute to the overall measure of the performance.

As shown by the quoted diagrams, the choice should fall on couples of the kind:

$$\alpha = \frac{23\pi}{120} \quad \text{or} \quad \alpha = \frac{11\pi}{60},\ \varphi = \frac{\pi}{9} \quad \text{or} \quad \varphi = \frac{2\pi}{15},$$

having a radar diagram enclosing a smaller surface, which should then be considered, if not optimal for all circumstances, at least having good performances in all cases when the six chosen criteria are almost equally important. (The first three smallest surfaces are those of the vaults $\alpha = \frac{23\pi}{120}, \varphi = \frac{\pi}{9}, \alpha = \frac{23\pi}{120}, \varphi = \frac{2\pi}{15}$, and $\alpha = \frac{11\pi}{60}, \varphi = \frac{2\pi}{15}$, in that order, for type A, and $\alpha = \frac{23\pi}{120}, \varphi = \frac{8\pi}{45}, \alpha = \frac{23\pi}{120}, \varphi = \frac{2\pi}{15}, \alpha = \frac{11\pi}{60}, \varphi = \frac{2\pi}{15}$, in that order, for type B.)

Entering into further details, assuming that a fast converging consolidation and the smallest thrust dominate on other criteria, the choice of the couple:

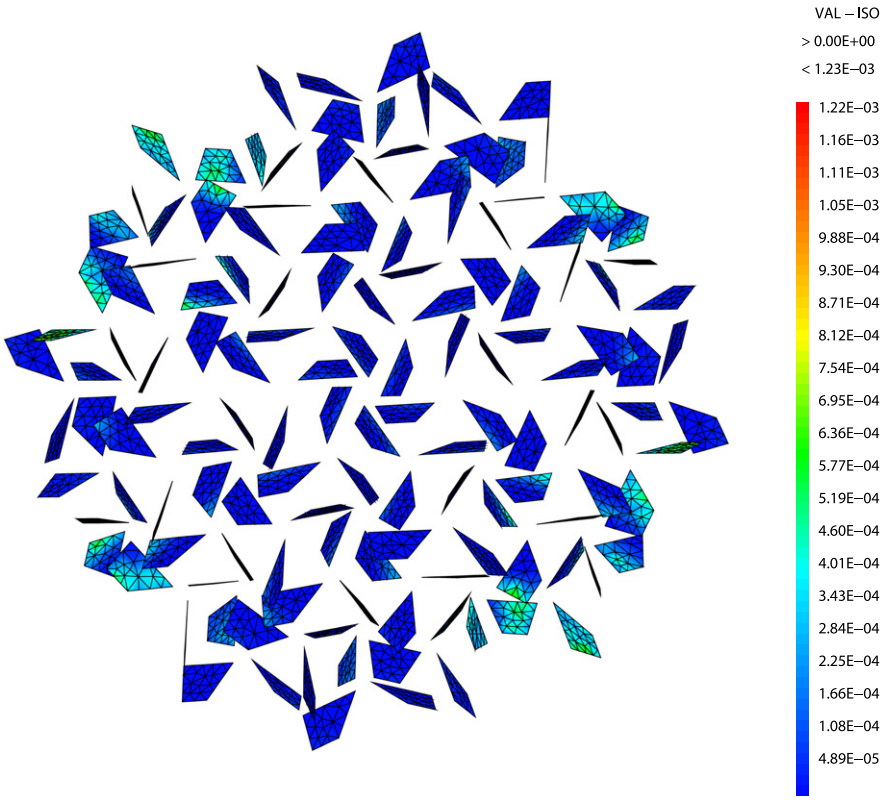

Fig. 34. The cumulated slip at joints after all loading cycles for type A, $\alpha = 23\pi/120$ and $\varphi = \pi/9$.

$$\alpha = \frac{11\pi}{60}, \quad \varphi = \frac{8\pi}{45}$$

is the most appropriate for a type A vault as it gives, among the cases with $\alpha \geqslant \frac{\pi}{6}$ that guarantees on the convergence of consolidation, the 1st result in terms of lightness, the 7th for the initial stiffness, and the 9th in terms of reduced thrust. Residual deflection is in this case larger than in all other cases bounded below by $\alpha = \frac{\pi}{6}$, but the cumulated plastic slip on joints is average for the family.

Always for type A vaults, the couple

$$\alpha = \frac{23\pi}{120}, \quad \varphi = \frac{\pi}{9},$$

having the radar diagram that encloses the smallest surface, can be considered as optimizing under the same set of reasons than the previous one, being in the average in terms of lightness and smallness of the thrust (excluding cases with $\alpha < \frac{\pi}{6}$ that consolidate slowly), 7th for the stiffness, and 2nd for the residual deflection and for the cumulated slip.

For vaults of type B it is the couple

$$\alpha = \frac{23\pi}{120}, \quad \varphi = \frac{2\pi}{15},$$

that gives the 1st result of all in terms of initial stiffness and, being for the self-weight and the thrust in the average of all cases with $\alpha \geqslant \frac{\pi}{6}$, can be taken as optimal.

In Figs. 33 and 34 we show the computed vertical deflection field and cumulated slip field at the joints, after all loading cycles, for the $\alpha = \frac{23\pi}{120}$ and $\varphi = \frac{\pi}{9}$ type A vault.

5. Fabrication information

For computer aided fabrications, especially 3D printing, Mathematica results can be exported in any necessary format; nevertheless we have focussed particularly on a traditional stone fabrication

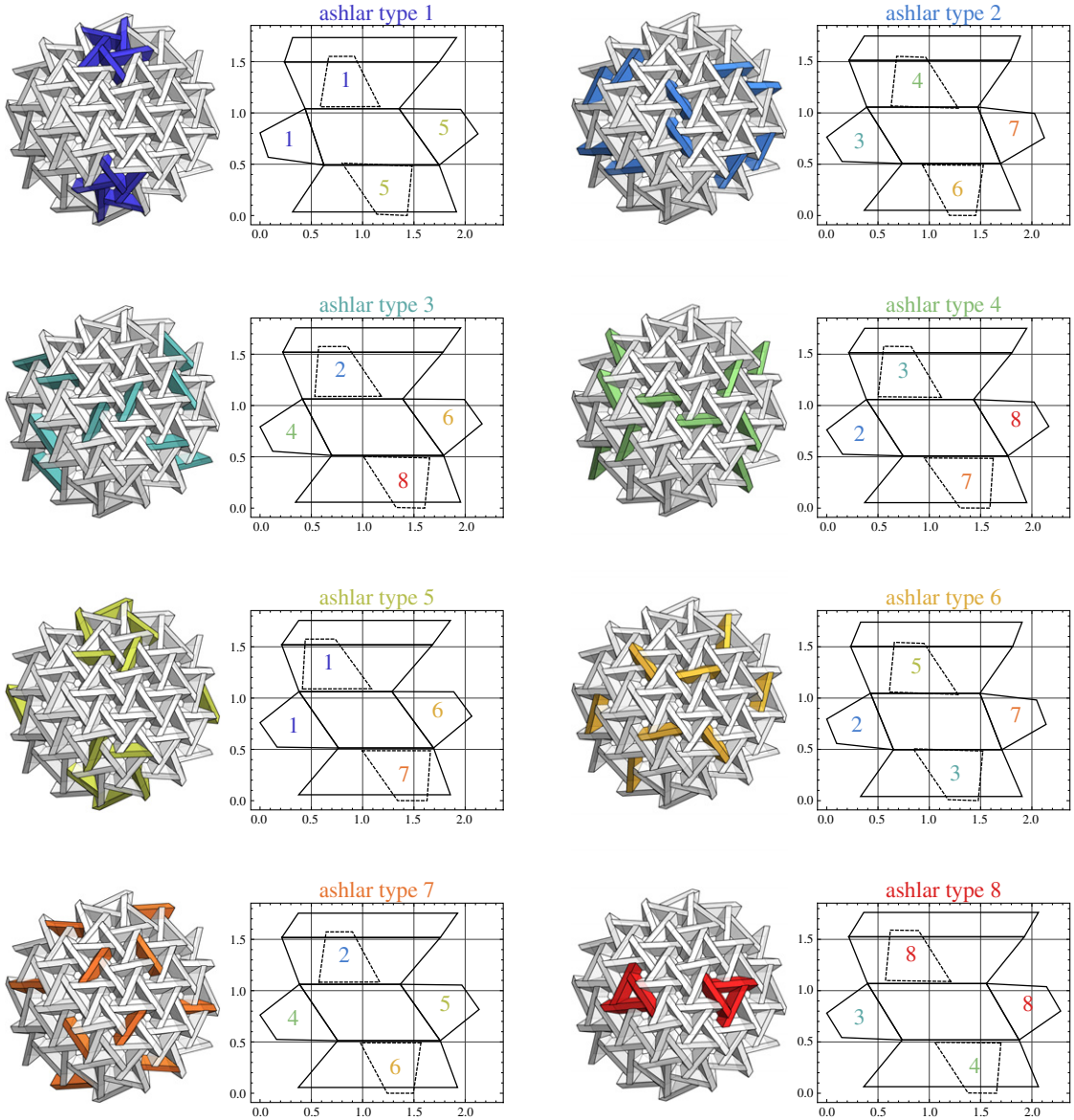

Fig. 35. Output of the net of the eight families of stones that compose the chosen optimal vault of type A, the $\alpha = \frac{23\pi}{120}$ and $\varphi = \frac{\pi}{9}$. Nets figures are developed on the plane of the face at the intrados and labeled with a colored text that corresponds to the color in the layout. Dashed lines represent the contour of the end-face of the stones that rest on sides of the portrayed one; the correct position of any stone can thus be determined during erection making its end-faces match such kind of prints on the neighboring ones. Colored numbers within some faces of the net correspond to the type of ashlar that is in contact with the given bloc on that face.

output, useful in experiments and for further technological analyses, and written automatic procedures to help in a standardization process.

First of all a classification of stones according to their geometry need be performed. For this purpose the net diagram of the polyhedral shape of each stone is produced automatically, taking the face of the ashlar at the intrados as a reference for the net. To speed up the procedure, this net is constructed only for type A vaults first. In the net the print of neighboring stones on the lateral surface of the ashlar is reproduced too. The simplification introduces no errors when studying type B vaults, as all geometric elements generating the final shape in this case are anyway taken into account when building type A vaults.

Then all such nets are compared and deemed to be equal if a difference smaller than a given precision (5 mm) is found between any equivalent coordinates of the two nets. In such a way ashlars are classed into families of equal shape and dimensions and subfamilies, when—shape and dimensions being equal—a different print of the neighbors is recorded.

In the particular cases that where studied, and thanks to the good regularity of the tessellation of the sphere that was used to generate the vault's geometry, only eight families are needed to class all 240 stones that compose an hemispherical vault. The eight of them enter the composition of the vault that was studied ($\zeta = 0.75$), actually made of 76 ashlars only.

Notice that there is no difference, within a given family, due to the print of neighbors on different members, i.e. all ashlars in a family are to be mounted in the same geometric conditions. This result ensues from the regularity of the geodesic sphere too.

After such classification, a polyhedral net for each of the eight families is constructed also for type B vaults, taking all 20 faces of the corresponding ashlars into account.

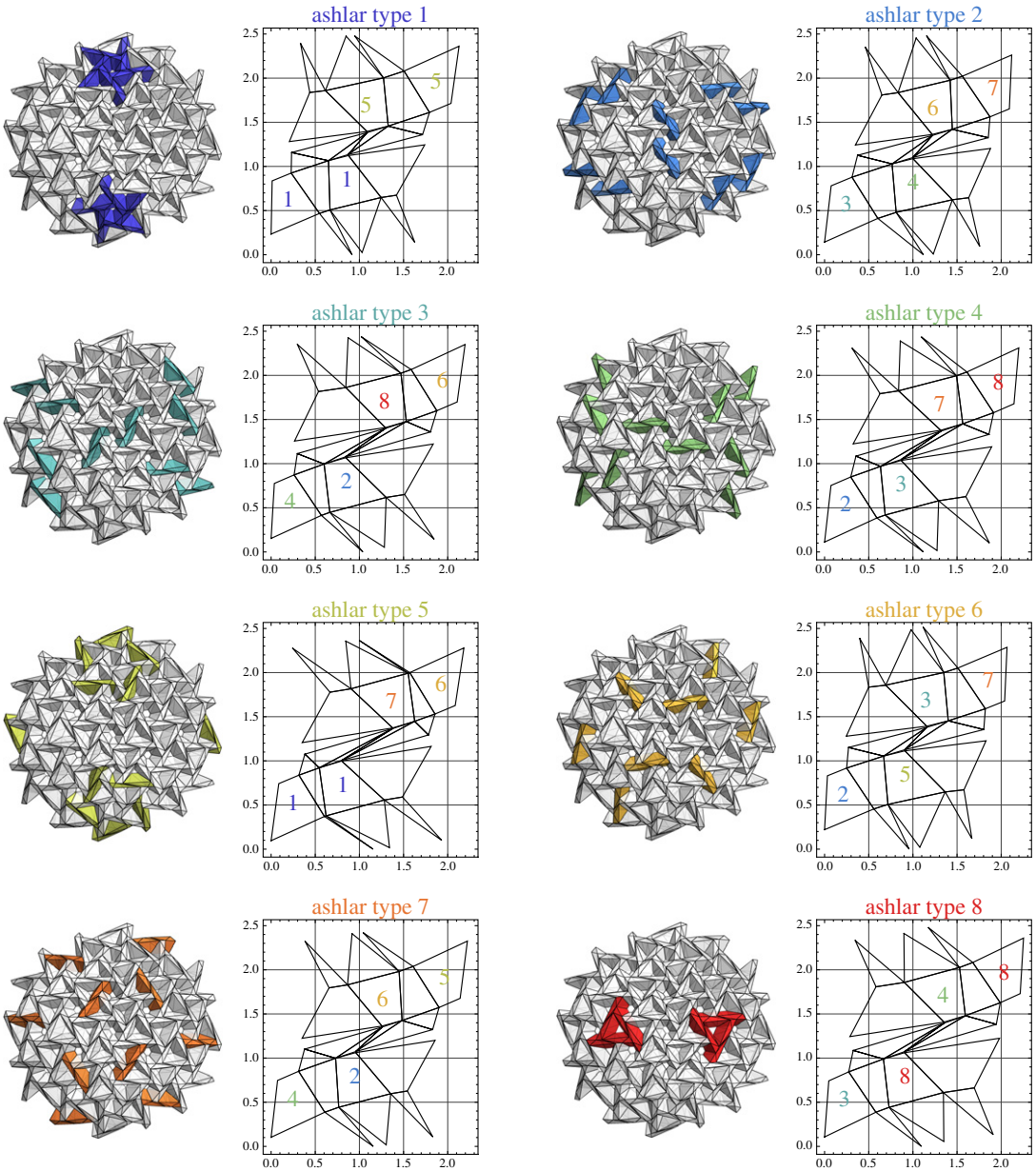

Fig. 36. Output of the net of the eight families of stones that compose the chosen optimal vault of type B, the $\alpha = \frac{23\pi}{120}$ and $\varphi = \frac{\pi}{9}$. Nets are developed on the plane of one of the faces at the extrados and labeled with a colored text that corresponds to the color in the layout. Colored numbers within some faces of the net correspond to the type of ashlar that is in contact with the given bloc on that face. The intrados face of blocs is split in the net and the triangles that compose it are attached alternatively to either lateral faces.

Finally, a color layout is produced to locate individual pieces in the vault according to the family they belong to. Fig. 35 shows a typical output for the $\alpha = \frac{23\pi}{120}$ and $\varphi = \frac{\pi}{9}$ type A vault. Fig. 36 shows the same output for the $\alpha = \frac{23\pi}{120}$ and $\varphi = \frac{\pi}{9}$ type B vault.

6. Conclusions

The procedure described in this paper makes a new family of structures accessible to the designer. They are called Abeille's domes in homage to the French engineer Joseph Abeille who invented the particular type of flat vault bond adapted here to generate domes.

Remarkably, the structural system is an hybrid between a vault and a nexorade, partly resisting by the principle of the inverted catenary, partly by that of the lever. Relying only on compressive strength and unilateral contact conditions, such system can prove advantageous if a reduction of the embodied energy is sought.

The solution of the geometrical issues related to the accommodation of a flat geometry on spherical surface are extended in this paper, with respect to what already presented in the literature, covering cases when the intrados and/or the extrados of the dome are convex polyhedral surfaces or smooth spheres.

Tools are also given for the evaluation of the mechanical performances and for an aid at the fabrication tasks. A finite element model of the structure has been set, with linear elastic ashlars and unilateral contacts with Mohr–Coulomb friction and associate slip. Numerical analyses have been run from parametrically generated inputs to test different structures and compare their behaviors. Two parameters were considered that are inherently related to Abeille's bond: the chirality angle, giving the extent to which the structure deviates from standard toward reciprocal frames, and the splice angle, measuring the opening of the wedge offered by the ashlars.

The structure has been tested numerically by submitting it to three sawtooth load-unload cycles. Computational outputs were compared on the base of: the increment of the residual deflection at the last loading step divided by the total residual deflection at the end of the last step; the maximum cumulated contact slip; the total residual deflection; the ratio between the tangent stiffness at the first loading ramp and the same measure taken at the last ramp; the initial overall compliance of the structure; the maximum side thrust at the vault's springing. To help choosing the optimal structure, a radar plot of the aforementioned criteria has been proposed and the parameters leading to the minimal area enclosed by the plot were selected as optimal.

Acknowledgements

This work was partly made during Ms. Mondardini doctorate within the framework of an industrial agreement for training through research (CIFRE) jointly financed by S.N.B.R., *Société Coopérative Ouvrière de Production*, and the National Association for Research and Technology (ANRT) of France.

References

Baverel, O., 2000. Nexorade: a family of interwoven space structure. Ph.D. thesis, University of Surrey.

Baverel, O., Nooshin, H., 2007. Nexorades based on regular polyhedra. Nexus Network Journal 9, 281–298.

Baverel, O., Nooshin, H., Kuroiwa, Y., Parke, G.A.R., 2000. Nexorades. International Journal of Space Structures 15, 155–159.

Brocato, M., 2011. Reciprocal frames: kinematical determinacy and limit analysis. International Journal of Space Structures 26, 343–358.

Brocato, M., Mondardini, L., 2011. Un sistema voltato di nuova concezione basato sull'apparecchiatura della volta piana di Joseph Abeille. In: D'Amato, C. (Ed.), Il progetto di architettura fra didattica e ricerca – Atti del primo congresso internazionale Rete Vitruvio. Polibapress, pp. 1941–1950.

Brocato, M., Mondardini, L., 2010. Geometric methods and computational mechanics for the design of stone domes based on abeille's bond. In: Advances in Architectural Geometry 2010. Springer, pp. 149–162.

Douliot, J.P., 1825. Traité spécial de coupe des pierres. Carilian-Gœury, Paris.

El-Raheb, M., 2010. Dynamics of a gravity stonewall. International Journal of Solids and Structures 47 (9), 1196–1208.

Emy, A.R., 1837. Traité de l'art de la charpenterie, vol. 1. Anselin and Carilian-Gœury, Paris.

Etlin, R., Fallacara, G., Tamborero, L., 2008. Plaited Stereotomy – Stone Vaults for the Modern World. Aracne Editrice, Roma.

Fallacara, G., 2006. Digital stereotomy and topological transformations reasoning about shape building. In: Dunkeld, M. (Ed.), Proc. Second Int. Congress Construction History. Queen's College Cambridge, Cambridge, pp. 1075–1092.

Fallacara, G., 2009. Toward a stereotomic design: experimental constructions and didactic experiences. In: Huerta, S. (Ed.), Proc. Third Int. Congress on Construction History. BTU Cottbus, Cottbus, pp. 553–559.

Fleury, F., 2009. Evaluation of the perpendicular flat vault inventor's intuitions through large scale instrumented testing. In: Huerta, S. (Ed.), Proc. Third Int. Congress on Construction History. BTU Cottbus, Cottbus, pp. 611–618.

Frézier, A.-F., 1737 reprint in 1980. La théorie et la pratique de la coupe des pierres et des bois pour la construction des voutes et autres parties des bâtiments civils et militaires. Jacques Laget L.A.M.E., Nogent-le-Roy.

Gallon, J.-G., 1735. Machines et inventions approuvés par l'Académie Royale des Sciences, depuis son établissement jusqu'à present; avec leur description. Martin-Coignard-Guerin, Paris.

Giordano, A., Mele, E., Luca, A.D., 2002. Modelling of historical masonry structures: comparison of different approaches through a case study. Engineering Structures 24 (8), 1057–1069.

Jean, M., 1999. The non-smooth contact dynamics method. Computer Methods in Applied Mechanics and Engineering 177 (3–4), 235–257.

Kenner, H., 1976. Geodesic Math and How to Use It. University of California Press, Berkeley.

Lourenço, P.B., Milani, G., Tralli, A., Zucchini, A., 2007. Analysis of masonry structures: review of and recent trends in homogenization techniques. Canadian Journal of Civil Engineering 34 (11), 1443–1457.

Nichilo, E.D., 2003. Learning from stone traditional vaulted systems for the contemporary project of architecture. The experimental construction site at the ponton de oliva. In: Huerta, S. (Ed.), Proc. First Int. Congress Construction History. Instituto Juan de Herrera, Madrid, pp. 743–754.

Pegon, P., 1999. Automatic generation of blocks connected with joints. Tech. Rep. JRC-Special Publication No. I.99.101, Joint Research Center.

Pegon, P., Pinto, A.V., Géradin, M., 2001. Numerical modelling of stone-block monumental structures. Computers & Structures 79, 2165–2181.

Rabasa-Dìaz, E., 1998. La bóveda plana de abeille en lugo. In: Bores, F. (Ed.), Actas del Segundo Congreso Nacional de Historia de la Construcción. Instituto Juan de Herrera, Universidad de A Coruña, Madrid, pp. 409–415.

Rafiee, A., Vinches, M., Bohatier, C., 2008. Application of the NSCD method to analyse the dynamic behaviour of stone arched structures. International Journal of Solids and Structures 45 (25–26), 6269–6283.

Sakarovitch, J., 2006. Construction history and experimentation. In: Dunkeld, M. (Ed.), Proc. Second Int. Congress Construction History. Queen's College Cambridge, Cambridge, pp. 2777–2791.

Suquet, P., 1983. Analyse limite et homogeneisation. Comptes Rendus de l'Academie des Sciences – Series IIB – Mechanics 296, 1355–1358.

Uva, G.R., 2003. Learning from traditional vaulted systems for the contemporary design. An updated reuse of flat vaults: analysis of structural performance and recent safety requirements. In: Huerta, S. (Ed.), Proc. First Int. Congress Construction History. Instituto Juan de Herrera, Madrid, pp. 2015–2021.

Yeomans, D., 1997. The serlio floor and its derivations. Architectural Research Quarterly 2, 74–83.